Asociación Argentina
de Mecánica Computacional

Mecánica Computacional Vol XXV, pp. 2267-2291
Alberto Cardona, Norberto Nigro, Victorio Sonzogni, Mario Storti. (Eds.)
Santa Fe, Argentina, Noviembre 2006

CHARACTERIZATION OF FLOW STRUCTURES AT THE FRONT OF CYLINDRICAL GRAVITY CURRENT FRONTS

Mariano I. Cantero[a,d], **Carlos M. García**[b], **Marcelo H. García**[c] **and S. Balachandar**[d]

[a]*Department of Geology, University of Illinois at Urbana-Champaign, 205 N. Mathews Ave., Urbana, Illinois 61801, USA, mcantero@uiuc.edu,* **http://www.geology.uiuc.edu**
[b]*Facultad de Ciencias Exactas, Físicas y Naturales, Av. Velez Sarsfield 1611, Universidad Nacional de Córdoba, Córdoba, Argentina, cgarcia2mjc@gmail.com,* **http://www.efn.uncor.edu**
[c]*Department of Civil and Environmental Engineering, University of Illinois at Urbana-Champaign, 205 N. Mathews Ave., Urbana, Illinois 61801, USA, mhgarcia@uiuc.edu,* **http://vtchl.uiuc.edu**
[d]*Department of Mechanical and Aerospace Engineering, University of Florida, 231 MAE-A, P.O. Box 116250, Gainesville, Florida 32611-6250, USA, bala1s@ufl.edu,* **http://www.mae.ufl.edu**

Keywords: Gravity current, density current, turbidity current, spectral methods, turbulence, environmental flows.

Abstract. Three dimensional direct numerical simulations are presented for cylindrical density currents using the Boussinesq approximation for small density difference. Three Reynolds numbers (Re) are investigated (895, 3450 and 8950, this particular choice corresponds to values of Grashof number of 10^5, 1.5×10^6 and 10^7, respectively) in order to identify differences in the flow structure and dynamics, and to compare with planar density currents. The simulations are performed using a fully de-aliased pseudospectral method. The simulated flows present the main features observed in experiments for the large Re. As the current develops, it transitions through different phases of spreading, namely acceleration, slumping, inertial and viscous. Soon after release the interface between light and heavy fluids rolls up forming Kelvin-Helmholtz vortices. The formation of the first vortex sets the transition between acceleration and slumping phases. Vortex formation continues only during the slumping phase. The coherent Kelvin-Helmholtz vortices undergo azimuthal instabilities and eventually breakdown into small scale turbulence. In the case of planar currents this turbulent region extends over the entire body of the current, while in the cylindrical case it only extends to the near-front region. The flow develops three-dimensionality right from the initial acceleration phase. During this phase, incipient lobes and clefts start to form at the lower frontal region. These instabilities grow in size and extend to the upper part of the front. Lobes and clefts continuously merge and split and, thus result in a complex pattern that dynamically evolves. The wavelength of the lobes grows as the flow spreads, while the local Reynolds number of the flow decreases. Due to the high resolution of the simulations, we have been able to link the lobe and cleft structure to local flow patterns and vortical structures. In the near front region and body of the current several hairpin vortices populate the flow. Laboratory experiments have been performed at the higher Reynolds numbers and the results have been compared to the simulation results. The agreement has been documented to be very good.

1 INTRODUCTION

Density (or gravity) currents are flows that are driven by horizontal pressure gradients generated due to the action of gravity over two different fluids with density difference (Allen, 1985; Simpson, 1997). In many real applications and laboratory experiments the current is canalized and is confined to flow between parallel lateral walls. In such situations, if the viscous effects of the lateral walls can be ignored, the current moves as a statistically two-dimensional (2D) flow with a nominally planar front (planar current). There are a number of other applications, such as the release of heavy gas into an open space, the collapse of an axisymmetric volcanic plume, or a point discharge into a lake or ocean, in which the gravity current is not channelized and is allowed to spread out over the entire horizontal plane. In such situations, the current moves as a statistically circular flow with a nominally cylindrical front (cylindrical current). Many examples of engineering, environmental and geological applications can be found in the books by Allen (1985) and Simpson (1997).

In a planar current the planform increases linearly with front location, while in a cylindrical current the planform increases quadratically. This fundamental difference dramatically decreases the intensity of the cylindrical current as it evolves. On the other hand, in a cylindrical current the concentrated vorticity at the head of the current initially intensifies as the current flows out due to intense vortex stretching (Patterson et al., 2006). These differences contribute to a distinct dynamics for the cylindrical currents. There are instances of directed release, for example heavier fluid released from a finite opening down a flat slope, where the current does not spread all around, but forms a conical planform. Density currents in such sector-shaped geometric tanks are often studied in the laboratory, instead of a full cylindrical current, due to their simplicity.

The dynamics of planar density currents is reasonably well understood (see for example Marino et al., 2005). Planar currents form a coherent front and a relatively long highly turbulent body behind the front (Cantero et al., 2006b). As the current spreads, it passes trough different phases, namely slumping, inertial and viscous (Huppert and Simpson, 1980). In the slumping phase the planar current moves at a nearly constant speed. The duration of the slumping phase depends on the initial volume and Reynolds number (Re) of the release. Provided the Re of the current is sufficiently large, the flow first enters an inertial self-similar phase (Rottman and Simpson, 1983) in which the current moves under the balance of buoyancy and inertial forces. In this phase the current's spreading rate (front velocity) scales as $t^{-1/3}$ (see for example Hoult, 1972). At later times, when viscous effects become important the current transitions to the viscous phase. In this phase the current's spreading rate scales as $t^{-5/8}$ if the dominant viscous effect arises from interfacial friction between the heavy and light fluids (Hoult, 1972) or as $t^{-4/5}$ if the viscous effect is primarily from bottom friction (Huppert, 1982).

In contrast to planar currents, as cylindrical currents spread they form a highly turbulent front and a relatively shallow calm body (Cantero et al., 2006a). Cylindrical currents are also thought to pass through a similar sequence of different phases of spreading. Provided the Reynolds number of the current is sufficiently high, after the slumping phase the current enters the self-similar inertial phase and the spreading rate scales as $t^{-1/2}$ (see for example Hoult, 1972). During the final viscous phase, the front velocity of the cylindrical current scales as $t^{-3/4}$ if the dominant viscous effect arises from interfacial friction (Hoult, 1972) or as $t^{-7/8}$ if the viscous effect is primarily from bottom friction (Huppert, 1982).

Several experiments have been performed to study the dynamics and structure of planar density currents. Allen (1971) and Simpson (1972) have devoted great effort to study the

lobe and cleft pattern observed at the front of planar density currents. Simpson and Britter (1979) studied the dynamics of the head of a gravity current. Huppert and Simpson (1980) and Rottman and Simpson (1983) have studied the different phases of spreading of a current produced by the release of a fixed volume of denser fluid in a lighter ambient. García and Parsons (1996) and Parsons and García (1998) have studied the similarity of planar density currents fronts, to mention but a few.

In comparison, experimental investigation of cylindrical currents has been relatively limited. Bonnecaze et al. (1995) analyzed the spreading rate and deposition patterns of cylindrical particle-driven gravity currents. Alahyari and Longmire (1996) performed Particle Image Velocimetry of a cylindrical gravity current and described the vortex dynamics in the early stages of the flow. Hallworth et al. (1996) studied experimentally the ambient fluid entrainment in 2D and axisymmetric currents. Hallworth et al. (2001) studied experimentally the effect of rotation on the propagation of cylindrical currents. Recent experiments in a sector-shaped tank for varying fractional depth of lease has been reported by Patterson et al. (2006).

Three-dimensional highly resolved simulations at modest Reynolds numbers have been performed for the planar currents (Lee and Wilhelmson, 1997a,b; Härtel et al., 2000b; Necker et al., 2002; Özgökmen et al., 2004; Cantero et al., 2006b). These simulations have provided a wealth of information, among other things, on the propagation speed of the current, the lobe and cleft structure of the head, and the turbulent structure of the body. Such detailed information for a cylindrical current over a range of Reynolds number is highly desired.

Here we center our attention on the release of a fixed cylindrical volume of homogeneous fluid in a slightly less dense environment and the time evolution of the resulting cylindrical current. We perform highly resolved simulations for 3D cylindrical currents at three different Reynolds numbers and document the results. We also compare the simulation results to experiments, where available.

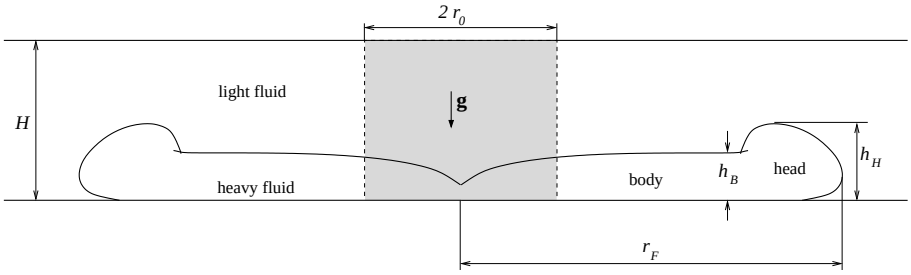

Figure 1: Sketch of a density current showing the main features of the flow and nomenclature for this work.

2 NUMERICAL FORMULATION

We consider flows in which the density difference is small enough for Boussinesq approximation to be valid. By this approximation density variations are only incorporated in the buoyant terms. The dimensionless equations read

$$\frac{\partial \tilde{u}_i}{\partial \tilde{t}} + \tilde{u}_k \frac{\partial \tilde{u}_i}{\partial \tilde{x}_k} = \tilde{\rho}\, e_i - \frac{\partial \tilde{p}}{\partial \tilde{x}_i} + \frac{1}{Re} \frac{\partial^2 \tilde{u}_i}{\partial \tilde{x}_k \partial \tilde{x}_k}, \tag{1}$$

$$\frac{\partial \tilde{u}_k}{\partial \tilde{x}_k} = 0, \qquad \text{and} \tag{2}$$

$$\frac{\partial \tilde{\rho}}{\partial \tilde{t}} + \frac{\partial}{\partial \tilde{x}_k} (\tilde{\rho} \tilde{u}_k) = \frac{1}{Sc\, Re} \frac{\partial^2 \tilde{\rho}}{\partial \tilde{x}_k \partial \tilde{x}_k}. \tag{3}$$

Here $\tilde{u}_i$ is the velocity vector, $\tilde{p}$ is the pressure, $\tilde{\rho}$ is the density, Re is the Reynolds number, Sc is the Schmidt number and e_i is a unit vector pointing in the gravity direction.

We have adopted the height of the fluid layer, H, as the length scale. Since there is no externally-imposed velocity scale for the flow, we have adopted

$$U = \sqrt{g'H} \tag{4}$$

as the velocity scale. Here $g' = g(\rho_1 - \rho_0)/\rho_0$, where g is the acceleration of gravity, ρ_1 is the density of the denser fluid and ρ_0 is the density of the ambient fluid. Consequently, the time scale is H/U. The dimensionless density and pressure are given by

$$\tilde{\rho} = \frac{\rho - \rho_0}{\rho_1 - \rho_0}, \qquad \text{and} \qquad \tilde{p} = \frac{p}{\rho_0 U^2}. \tag{5}$$

The two dimensionless numbers in equations (1)–(3) are, respectively, the Reynolds and Schmidt numbers, defined as

$$Re = \frac{U H}{\nu} = \frac{\sqrt{g' H^3}}{\nu} \qquad \text{and} \qquad Sc = \frac{\nu}{\kappa}, \tag{6}$$

where ν is the kinematic viscosity and κ is the diffusivity of temperature or chemical species responsible for the density difference. A cylindrical volume of height H (full-depth) and radius r_0 containing the heavier fluid is released into the surrounding lighter fluid. Figure 1 shows the nomenclature used in this work and the initial setting of the flow. In this work we will concentrate on the condition $r_0 = H$.

The computational domain is a rectangular box of size $\tilde{L}_x \times \tilde{L}_y \times \tilde{L}_z$. Since the current spreads radially outward along the entire $\tilde{x} - \tilde{y}$ plane we choose $\tilde{L}_x = \tilde{L}_y$. Periodic boundary conditions are employed along the $(\tilde{x})$ and $(\tilde{y})$ directions and thus here we approximate a doubly periodic array of cylindrical gravity currents with a lateral spacing of $\tilde{L}_x = \tilde{L}_y$ along the horizontal directions. At the top and bottom walls no-slip and zero-gradient conditions are enforced for velocity and density, respectively. The planform of the periodic box is taken to be 15×15 in order to allow unhindered development of the current for sufficiently long time. The interaction of the radially advancing front with the adjacent currents across the periodic boundaries becomes significant only as the front reaches within 1 dimensionless unit from the boundaries (Härtel et al., 2000b; Cantero et al., 2006a). The flow was started from rest with a minute random disturbance prescribed in the density field. The details of the initial conditions can be found in Cantero et al. (2006a). The governing equations are solved using a de-aliased pseudospectral code whose details can be found in Cantero et al. (2006b).

In this work, three different Re are considered: $Re = 895$, 3450 and 8950. The corresponding Grashof number, defined as $Gr = Re^2/8$ are 10^5, 1.5×10^6 and 10^7, respectively. The intermediate Reynolds number corresponds to that considered by Härtel et al. (2000b) in the planar configuration. With increasing Re the complexity of the flow increases, and this required increased resolution. The grid resolution employed for the three different simulations are $280 \times 280 \times 72$, $512 \times 512 \times 110$ and $880 \times 880 \times 180$ and thus they involve, 5.6, 28.8 and 139.4 million grid points. The numerical resolution for each simulation was selected to have between 6 and 8 decades of decay in the energy spectrum for all the variables. The time step was selected to produce a Courant number smaller than 0.5. The simulation at $Re = 8950$ required about 1 month of continuous run on 64 processors of the new SGI Altix 3000 (put to production on April 2005 at NCSA, University of Illinois at Urbana-Champaign), about 70Gb

of RAM memory to run, 600Gb of storage for raw data, and 18Tb (18000 Gb) of storage for visualization postprocessing made by NCSA scientists.

In the planar case, along the spanwise direction, the width of the periodic domain is typically chosen to be 1.5 dimensionless units, which is adequate to include several spanwise lobe and cleft structures (Härtel et al., 2000a). Thus the present simulations of the cylindrical current are an order of magnitude more computationally expensive than the planar simulations, for similar Reynolds number and grid resolution. By imposing symmetry along the $\tilde{x} = 0$ and $\tilde{y} = 0$ planes the computational domain and correspondingly the computational cost can be reduced by factor 4 (Patterson et al., 2006). However, in the context of the present spectral simulations, it is more complex to impose such symmetry boundary conditions. Despite the increased computational cost there are advantages with the larger domain. First, if there are low circumferential wavenumber ($k_\theta = 1$ or 2) instabilities in the propagation of the front, such instabilities can only be captured in the larger domain, without imposed symmetries. The initial perturbation included a wide range of circumferential modes. Thus, the present simulations will capture the low wavenumber instabilities if they are present in a real system. If the computed results do not show such low wavenumber undulation in the propagation of the front, then these modes are not important and the use of symmetry boundary conditions will be supported. Furthermore, in the initial perturbation we make sure that the evolution of the current in the four quadrants is dissimilar. The evolution of the current in the four different quadrants, although statistically identical, are not exactly the same. Thus, at the higher Re turbulent flows, we have four times larger data base for more accurate extraction of the statistics.

3 RESULTS AND DISCUSSION

3.1 Roll up of the interface

3.1.1 $Re = 895$

After the release of the denser fluid, an intrusive front forms. Figure 2 shows the structure of the current as visualized by a density isosurface of $\tilde{\rho} = 0.15$ for the lower Re of 895. The figure shows only one quarter of the computational domain to allow for better visualization of the flow structures. Two different dimensionless time instances are shown, $\tilde{t} = 7$ and 10. At both times a well-defined head of the current can be seen. The head initially consists of a coherent anti-clockwise rotating vortex ring (marked A1 on the $\tilde{x} - \tilde{z}$ plane in figure 2) that forms first due to the roll up of the interfacial shear layer between the heavy and light fluids. As the front of the current progresses radially out, the vortex ring A1 slightly lifts up above the ground and a new anti-clockwise vortex ring A5 (numbering will become clear below) forms ahead of it. At the earlier time of $\tilde{t} = 7$, the presence of two different vortex rings, one behind the other, can be clearly observed and together these two vortex rings form the distinct raised head of the current seen in the density isosurface. At this Re the currents remains axisymmetric at all times and the initial non-axisymmetric disturbance introduced into the flow decays away quickly.

3.1.2 $Re = 3450$

Figure 3 shows the structure of the current at the intermediate Re of 3450. At the earlier time of $\tilde{t} = 7$ a sequence of four vortex rings, one right behind the other, can be seen. The anti-clockwise vortex marked A1 is the first one to form, as a result of the roll up of the interface that develops soon after the release of the heavy fluid. With increase in time, the front of the heavy fluid propagates radially out, while the front of the light fluid propagates back towards the axis.

As new interface develops, subsequent roll up of the interface results in the formation of vortex ring A2. In the present case the back propagating disturbance reaches the axis by about $\tilde{t} = 3$, after which the mean interface between light and heavy fluids increases only due to the forward propagation of the heavy front. Also at around $\tilde{t} \approx 3.0$ the interface begins to roll up again to form the third vortex ring A3. These later vortices can be observed to be progressively weaker than the first one. We observe no further roll up of the interface into coherent vortex rings. At the earlier time of $\tilde{t} = 7$ the three vortices A1, A2 and A3 are nearly equispaced. The formation of vortex ring A5 ahead of A1 will be discussed below in the context of the higher Re case. By about $\tilde{t} \approx 10.0$ the vortex rings A1 and A5 merge and form a single head of the current, which can be observed at the later time of $\tilde{t} = 14$ shown in figure 3. Also at this time, due to their faster propagation, we observe the combined vortex ring A1+A5 is farther ahead of the weaker vortex rings A2 and A3.

At this Re the initial disturbance introduced into the flow grows over time and quickly the flow forms a lobe-and-cleft structure. The initial random disturbance introduced at the interface includes a wide range of circumferential modes. It is, however, clear from the figure that there is a preferred most amplified circumferential mode of instability. At the earlier time about 20 lobe and cleft structures can be observed within the quadrant that is visualized, while at the later time slightly lower number of lobe and cleft structures are observed. At the early time the instability can be observed only at the head of the current, but at later time the instability is not limited to only the head of the current, and it can be clearly observed along the subsequent vortex rings as well. The lobes and clefts are observed to be reasonably well organized at the earlier time, while at the later time their structure is less regular, suggesting the strong role of nonlinearity. The height of the current is elevated only at the location of the vortex rings. In between the vortex rings the current appears to be relatively thin and calm and devoid of strong instabilities. The remnant heavy fluid observed along the axis ($\tilde{x} = \tilde{y} = 0$) and near the top boundary are artifacts of the no-slip boundary condition applied at the top boundary. But changing this to a free slip top boundary does not alter the physics of the current to be discussed below.

3.1.3 $Re = 8950$

Figure 4 shows the time development of the flow structure for the higher Re of 8950. Initially, the flow evolves as a nearly axisymmetric flow in which Kelvin-Helmholtz rolls develop and form along the front and body of the current (Cantero et al., 2006a). At this time of $\tilde{t} = 2.7$ the front nose of the current is slightly lifted away from the bottom wall and, as a consequence of no-slip condition, a layer of light fluid penetrates below the raised nose resulting in unstable stratification. It can be observed that at this early time some incipient lobes and clefts are starting to form. However, the three-dimensionality is primarily limited to the nose of the current.

The roll up process of the interface can be better observed from circumferentially-averaged variable plots. For any flow variable f, the circumferential-average is indicated by an overbar and computed as

$$\bar{f}(\tilde{r}, \tilde{z}) = \frac{1}{2\pi} \int_0^{2\pi} f(\tilde{r}, \theta, \tilde{z})\, \mathrm{d}\theta. \tag{7}$$

In figure 5 circumferentially-averaged velocity vector plots are presented at several time instances. To allow better visualization of the rolled up vortices, the velocity field is plotted in a frame of reference moving with the front of the current together with contours of constant density. The interface between the heavy and light fluids is taken to be marked by $\tilde{\rho} = 0.15$.

At the earliest time shown ($\tilde{t} = 1.77$) only the incipient roll up of the anti-clockwise vortex ring A1 can be seen. By $\tilde{t} = 2.7$ the back propagating front has almost reached the axis and in addition to the initial vortex ring A1, two additional anti-clockwise vortex rings A2 and A3 can be observed upstream. Also, as a consequence of the bottom no-slip boundary condition, the strong anti-clockwise vortex ring A1, results in the formation of a clockwise rotating vortex ring C1 closer to the bottom wall. At $\tilde{t} = 3.54$ the pair of vortex rings A1 and C1 form the head of the current. Vortex rings A2 and A3 have merged and have resulted in the formation of the clockwise vortex ring C2. A new rolled up anti-clockwise vortex A4 and the associated clockwise vortex ring C3 can be seen as well. The resulting vortex ring structure and the interface can be verified in figure 4. The presence of counter-rotating vortices has been observed in cylindrical gravity currents in the experiments of Alahyari and Longmire (1996). They interpreted them as boundary layer separation caused by the adverse pressure gradient produced by the anti-clockwise vortex rings formed.

By $\tilde{t} = 5.31$ an important development has occurred. The effect of C1 is to lift the dominant vortex ring A1 further away from the bottom wall. This lift up lowers the outward propagation velocity of the vortex ring. The front thus advances faster than the vortex ring A1 and results in the formation of a new anti-clockwise vortex ring A5, downstream of A1. This mechanism is the cause of vortex ring marked A5 in the two lower Re cases as well. As the flow evolves, instabilities grow and destabilize the Kelvin-Helmholtz rings, which suffer strong stretching and bending in the azimuthal direction. By $\tilde{t} = 7$ a fully developed pattern of lobes and clefts can be observed at the front, but the vortex rings have decayed to smaller and weaker vortices. At $\tilde{t} = 21$ only A5 that forms the front of the current and the remnant of the original vortex ring A1 can be observed. Despite the decay, the lobe and cleft pattern is still present. The level of turbulence has decayed substantially and only the front of the current presents some vortical structures. The body of the current has become a relatively calm region, where most of the flow features manifest as interfacial waves.

3.2 Interface circulation estimates

The roll up of the flow into coherent vortex rings is clearly associated with vorticity (or circulation) at the interface. A rough estimation of circulation at the interface will be pursued for the circumferentially averaged flow in order to understand the roll up process. The (circumferentially averaged) velocity jump across the nearly horizontal interface between light and heavy fluids is proportional to the (circumferentially averaged) velocity of the propagating front, $\overline{u}_F(\tilde{t})$. The constant of proportionality is 1.0 for a deeply submerged current and is equal to 2.0 for a current of height half the layer depth and for all other intermediate current depths the constant of proportionality is between 1.0 and 2.0. Net circulation at the (circumferentially averaged) interface is then

$$\Gamma(\tilde{t}) \sim \overline{u}_F(\tilde{t})\overline{l}_F(\tilde{t})\,, \tag{8}$$

where $\overline{l}_F$ is the length of the current. If we assume a $\overline{u}_F \sim \tilde{t}^{\,\beta}$ behavior for the (circumferentially averaged) front velocity, then we obtain the following power-law evolution for circulation

$$\Gamma(\tilde{t}) \sim \tilde{t}^{\,2\beta+1}\,. \tag{9}$$

It can be readily seen from the equation above that only for $\beta > -1/2$, net circulation at the interfaces increases with time. If the front velocity decays more rapidly (i.e., for $\beta < -1/2$), then net circulation at the interface decreases.

In a cylindrical current during the slumping phase were the front moves at a constant velocity, then corresponding $\beta = 0$, and as a result in this phase net vorticity will increase as $\tilde{t}$. In the inertial phase, where the gravitational and inertial forces are in approximate balance, the asymptotic behavior of the cylindrical current is given by $\overline{u}_F \sim \tilde{t}^{-1/2}$ (Fay, 1969; Fannelop and Waldman, 1971; Hoult, 1972; Huppert and Simpson, 1980). Thus, in the inertial phase the circulation at the interface can be expected to stay constant ($\Gamma(\tilde{t}) \sim \tilde{t}^0$). In the viscous phase, where the gravitational and viscous forces are in approximate balance, two different power-law solutions can be obtained depending on the importance of interfacial friction between the heavy and light fluids versus friction at the bottom wall. In the case of former, the power-law solution for a cylindrical current is $\overline{u}_F \sim \tilde{t}^{-3/4}$ (Hoult, 1972), and for the later self-similar solution yields $\overline{u}_F \sim \tilde{t}^{-7/8}$ (Huppert, 1982). Both these viscous phase solutions predict a decrease in interfacial circulation as either $\tilde{t}^{-1/2}$ or $\tilde{t}^{-3/4}$. Based on above argument, one can anticipate interface to strengthen and continue to roll up into vortex rings in the slumping phase. The interface roll up remain constant during the inertial phase and eventually decrease during the viscous phase.

Figure 6 show the log-log plot of velocity of the front as a function of time for the three different Re. Also show in the figure are the $\tilde{t}^{-1/2}$, $\tilde{t}^{-3/4}$ and $\tilde{t}^{-7/8}$ power-laws (which are straight lines in the log-log plot) corresponding to the inertial phase and the two viscous phase predictions, respectively. Although a perfect constant velocity is not observed, a brief period of slow variation in velocity is observed, which can be taken to be the slumping phase of a cylindrical current (Cantero et al., 2006b). From this figure it can be identified that the lower Re flow transition directly from the slumping to the viscous phase, while the higher two Re flows transition from the slumping to the inertial and eventually to the viscous phase. The corresponding transition times can be estimated from the figure to be $\tilde{t} \simeq 5$ for the slumping/viscous transition for the lower Re flow, and $\tilde{t} \simeq 5$ for the slumping/inertial transition and $\tilde{t} \simeq 9$ for the inertial/viscous transition for the higher two Re flows.

In Cantero et al. (2006b) it was observed that the formation of the first vortex ring (A1) marked the start of the slumping phase after a short acceleration period of the flow (acceleration phase). Here we note that the formation and intensification of all new anti-clockwise vortex rings happens over $\tilde{t} < 5$ for all Re (during the slumping phase). The number of vortex rings that form in a cylindrical current is primarily a function of both Re and the volume of release. With increasing volume of heavy fluid at release, the time spent in the slumping phase increases and during these period circulation at the interface continues to increase. With increasing Re the frequency at which the interface rolls up to form coherent vortices increases. At $Re = 895$ only one vortex ring (A1) forms in the slumping phase. At $Re = 3450$ and 8950 three and four vortex rings form, respectively, before the inertial phase. In all the case, the only exception is vortex ring A5 that forms ahead of the primary vortex ring A1.

In a cylindrical current, as the current radially propagates out the vortex rings are stretched. Circulation within the vortex is preserved, but stretching tends to intensify the vortex by decreasing its cross-section. The resulting long and thin vortex experiences stronger diffusion and dissipation.

3.3 Qualitative experiments

For comparison, we have also performed laboratory experiments in a rectangular tank of $2m \times 2m \times 0.5m$. At one corner of the box a quarter cylinder of radius $0.165m$ is filled with salt water of slightly higher density. The rest of the tank is filled with fresh water and the two are initially separated with a cylindrical lock. Both the fresh and salt water are maintained to the same height of $0.165m$ and therefore here we consider a full-depth release with $r/H = 1$.

The salt water is also dyed with potassium permanganate in order to visualize the front as it propagates out. The present experiment can thus be considered as a cylindrical current in a 90° sector. Density difference and the height of the layer are chosen to yield a Reynolds number of 8950, and thus the results can be directly compared against those presented in figure 4. The bottom of the tank presents a smooth no-slip surface for the flow and the free surface at the top presents a slip condition. In the experiment, the heavy fluid is released in a finite amount of time (the time to lift the gate) and thus, the initial condition is not exactly the same as in the simulations. Despite the differences in the experimental set up and the numerical simulation, the results resemble very closely. Figure 6 shows the front velocity from simulations and for the present experiment in very good agreement. Also, the lobe and cleft pattern is qualitatively well captured by our simulation. Figure 7 shows the lobe and cleft pattern from the experiment for four time instances when the front is located at approximately $\tilde{r} = 3.6, 4.1, 4.5$ and 5.0. Each frame shows the complete front (that is the $\pi/2$ circular sector) of the current in the experiment. Through postprocessing of the images, the lobe and cleft pattern could be clearly demarcated. Lobes are indicated with arrows to allow for a quantitative comparison with experiments. Note that the Schmidt number for salt in water is 700, while the computations employ $Sc = 1$. This offers some justification to findings that as long as $Sc > \mathrm{O}(1)$ the flow and the lobe and cleft pattern are not very sensitive to the precise value of Sc (Härtel et al., 2000b; Cantero et al., 2006a).

3.4 Lobes and cleft

The 3D lobe and cleft structure of the advancing front can be seen in figures 3 and 4 for the larger two Re considered in this paper. The circumferential variation in front propagation continues after the initial formation of lobes and clefts and, as a result, the number and location of lobes and clefts constantly rearrange along the front. The front of the current identified by contour of $\tilde{\rho} = 0.015$ at the bottom boundary is plotted on the $\tilde{x} - \tilde{y}$ plane (top view) in figure 8. The front location at several equispaced time intervals of $\Delta\tilde{t} = 0.354$ are superposed for $Re = 3450$ (frame (a)) and $Re = 8950$ (frame (b)). The composite picture provides a clear view of the formation of lobes and clefts and the footprint the clefts leave on the horizontal $\tilde{x} - \tilde{y}$ plane as the front advances over time. At the beginning (toward the center of the figure) the front is nearly axisymmetric, but small random disturbances introduced in the initial condition quickly develop into well-formed lobe and cleft structures. Different instability mechanisms for the formation of lobe and cleft structure of the front have been proposed in the context of planar currents (Allen, 1971; Simpson, 1972; Härtel et al., 2000a). These mechanisms are likely to be active and responsible for the lobe and cleft structure of the cylindrical currents as well. Nevertheless, the formation of lobes and clefts is due to circumferential variation in the speed of the current. Even after they are fully formed, the speed of the current continues to vary along the circumference of the front, thus resulting in repeated splitting and merging of existing lobes and clefts. A complex pattern is etched by the clefts as the front advances, with repeated formation of new ones and merger between older ones, which is well captured in figure 8.

Figure 9 shows details of the lobe and cleft pattern observed in the present experiments performed at $Re = 8950$.The figure shows the front of the current when it is located at $\tilde{r} \simeq 6.5$. At this late time the concentration of potassium permanganate at the front has decreased enough to permit clear visualization of the lobes and clefts in the flow. In the photographs, long streaks of fresh clear water trapped between the bottom of the tank and the current can be clearly identified. These streaks mark the path traversed by the clefts and has been demarcated in the figure with dashed lines to help their visualization. The photograph not only provides information on

the instantaneous structure of the front, but also captures the path etched by the clefts in the recent past. Thus the experimental photograph can be compared with the computation result presented in figure 8 and the qualitative features are in agreement. For example, what appears to be initiation of new clefts and merges between existing clefts (marked with arrows) can be observed in the figure.

Quantitative information on the lobe and cleft structure for both $Re = 3450$ and 8950 are presented in Table 1. At several selected time instances the mean radial location of the front ($\overline{r}_F$), the front velocity ($\overline{u}_F$), the current head height ($\overline{h}_H$), the local instantaneous Reynolds number of the front ($Re_F = Re\,\overline{h}_H\overline{u}_F$), the mean number of lobes observed within a 90° sector (N_{90}), and the mean wavelength of the lobe ($\tilde{\lambda}_l = \pi\overline{r}_F/2N_{90}$) are presented in the table. Also presented in the table are wavelength of the lobe extracted from the present experiment at $Re = 8950$ (see figure 7), as well as other available experimental and computational information for the planar case. The counting of lobes from figures 7 and 8 is subject to some variation. Especially at instances of incipient mergers and splitting the number of lobes to be counted is subject to some interpretation. In table 1 the number of lobes is therefore presented with an error bar. In addition to counting we have also computed both Fourier spectra and two-point correlation of the front location as a function of θ. Due to the complex nature of the front, both the spectrum and the correlation present a set of broad peaks. Nevertheless, their results are consistent with those obtained from simple counting.

The amplitude of disturbance introduced in the initial condition is the same at all Re. So from figure 8 it can be seen that at the higher Reynolds number the disturbance grows more rapidly and results in earlier formation of distinct lobe and cleft structure. At both Re the number of lobes initially goes through a brief period of adjustment where N_{90} first increases flowed by some reduction. After this initial adjustment the number of lobes continue to increase with time. The increase is more prominent for $Re = 3450$, while at the higher Re of 8950 the increase is only modest. At $Re = 8950$ an increased competition for lobes to grow can be observed. For example, one can observe in figure 8 instances where a new lobe that forms grows to a small size (smaller than the mean), but gets erased through merger, before it reaches maturity. Furthermore, careful observation of the details in figure 8(b) shows instances where out of a single lobe multiple smaller lobes are formed. Soon, all but one get killed, and only one grows to the mean size. In contrast, at the lower Re of 3450 almost every lobe that is born, grows to maturity and reaches the mean size of a lobe for that radial location as can be seen from figure 8(a). Typically, a lobe splits into two with both growing over time. There is, however, lobes merging as can be seen in the details of figure 8(a), but this process is less intense than in the case of $Re = 8950$. In terms of wavelength, the size of the lobes continues to steadily increase over time.

Figure 10 shows a snapshot of the near-bed flow at the front of the current for $Re = 3450$ at $\tilde{t} = 21$. The inset in the figure indicates the location of the horizontal section at $\tilde{z} = 0.04$ relative to the front where the flow is shown. The front is visualized by the density contour of $\tilde{\rho} = 0.015$ at the bottom wall (denoted by a thick solid line). The vector field shows the horizontal flow (velocity components $\tilde{u}_x$ and $\tilde{u}_y$), and the contour lines show the vertical flow (solid line: positive $\tilde{u}_z$, and dashed line: negative $\tilde{u}_z$). The vector field shows clearly that the horizontal flow in the clefts is slower that in the lobes, and that there is a circumferential component that directs from the center of the lobes into the clefts. This flow pattern had been postulated by Allen (1985). The contours of vertical velocity show ascending flow at the clefts and descending flow at the lobes. The composition of these results shows that each lobe has a pair of counter rotating vortices as originally postulated by Allen (1985). Some evidence of

Source	Re	$\tilde{t}$	$\overline{r}_F$	$\overline{u}_F$	$\overline{h}_H$	Re_F	N_{90}	$\tilde{\lambda}_l$	Phase
DNS - C	3450	3.9	2.4	0.36	0.4	499	16±2	0.24	SP
DNS - C	3450	5.3	2.9	0.32	0.26	283	19.5±2	0.24	IP
DNS - C	3450	7.1	3.4	0.26	0.33	291	20.25±2	0.27	IP
DNS - C	3450	10.6	4.2	0.22	0.354	266	18±2	0.36	IP
DNS - C	3450	14.1	5	0.2	0.32	221	19.5±2	0.4	IP
DNS - C	3450	17.7	5.7	0.18	0.27	167	20.5±2	0.44	VP
DNS - C	3450	21.2	6.3	0.15	0.25	129	22.3±2	0.44	VP
DNS - C	3450	24.8	6.8	0.12	0.23	99	25±2	0.42	VP
DNS - C	8950	1.8	1.7	0.41	0.3	1098	26.25±3	0.1	SP
DNS - C	8950	3.5	2.4	0.38	0.36	1226	30.5±3	0.12	SP
DNS - C	8950	7.1	3.6	0.29	0.29	774	25.25±3	0.22	IP
DNS - C	8950	10.6	4.5	0.25	0.32	711	27±3	0.26	IP
DNS - C	8950	14.1	5.3	0.22	0.28	542	27.25±3	0.31	IP
DNS - C	8950	17.7	6	0.19	0.27	446	27.5±3	0.34	VP
DNS - C	8950	20.9	6.6	0.14	0.25	301	28.25±3	0.37	VP
EXP - C	8950		3.6				25±3	0.23	
EXP - C	8950		4.1				28±3	0.23	
EXP - C	8950		4.5				29±3	0.24	
EXP - C	8950		5				31±3	0.25	

Table 1: Quantitative information on the lobe and cleft structure. In the table: $\overline{r}_F$ is the mean radial location of the front, $\overline{u}_F$ is the front velocity, $\overline{h}_H$ is the current head height, $Re_F = Re\,\overline{h}_H\overline{u}_F$ is the local instantaneous Reynolds number of the front, N_{90} is the mean number of lobes observed within a 90° sector, and $\overline{\lambda}_l = \pi\overline{r}_F/2N_{90}$ is the mean wavelength of the lobe. C refers to cylindrical currents and P to planar currents. †Most unstable wavelength computed from initiation of lobe and cleft structure from figure 11 in Simpson (1972). ‡Most unstable wavelength computed from figure 6 in Härtel et al. (2000a).

vortical activity at the front of the current can be seen in figure 11, which will be discussed in detail in section 3.5.

3.5 Turbulent structures

The complex 3D vortical structure of the current is not entirely apparent in the density isosurface presented in figure 4. The corresponding isosurface of *swirling strength* at the later three times are shown in figure 11. Here the swirling strength, $\tilde{\lambda}_{ci}$, is defined as the absolute value of the imaginary portion of the complex eigenvalues of the local velocity gradient tensor. As discussed in Zhou et al. (1999) and Chakraborty et al. (2005) the swirling strength provides a clean measure of the compact vortical structures of the flow. Swirling strength picks out regions of intense vorticity, but discriminates against planar shear layers, where vorticity is balanced by strain-rate. As can be seen from figure 11, the 3D vortical structure of the high Re current is well extracted by $\tilde{\lambda}_{ci}$.

The root mean square of the swirling strength within the vortical region at the three different times are 1.05, 0.93 and 0.32, respectively. The isosurface of $\tilde{\lambda}_{ci} = 2.12$ is plotted in figure 11 and thus the figure captures only the intense vortical regions of the flow.

At the first instance shown in figure 11, the strong vortical structures extracted by $\tilde{\lambda}_{ci}$ near the head of the current are associated with the Kelvin-Helmholtz vortex rings A1 and A5. The effect of lobes and clefts on the vortical structure can be clearly observed. Two other rings of intense turbulence can be seen. The one centered around $\tilde{r} \approx 1.75$ is associated with the merged vortex ring A2+A3. The final weaker ring of turbulent structure is associated with vortex ring A4. By $\tilde{t} = 14$, all except the vortex ring associated with the front of the current have already decayed and any turbulence associated with them are no longer captured by $\tilde{\lambda}_{ci} = 2.12$. However this is an artifact of the relatively high threshold of 2.12 set for visualization. Also plotted in figure 11 for $\tilde{t} = 21$ is isosurface of $\tilde{\lambda}_{ci} = 0.35$. From the figure it is clear that active turbulence is not just limited to the vortex rings. A low level of turbulence can be observed behind the vortex rings. In addition we observe turbulence associated with a second vortex ring (A2+A3) located at $\tilde{r} \approx 3.75$ and close to the origin.

Apart from the vortex rings and the lobe and cleft structure the turbulent region of the flow behind the head is dominated by inclined vortical structures and several hairpin vortices can be observed (see for example inset for $\tilde{t} = 14$). These structures are similar to those observer in a turbulent wall layer, where the vortical structures are tilted from the wall in the flow direction. In case of cylindrical gravity current the flow is directed radially out. However, in a frame of reference moving with the front, the flow within the current is radially inward, which explain the observed orientation of the vortical structures within the current. Similar trains of inclined vortical structures were observed for the case of planar gravity currents as well (Cantero et al., 2006b). The difference, however, is that at the present Re in the planar current the region of turbulence extended over a large portion of the body of the current, while in the cylindrical case the turbulence is limited to only vortex rings and the head of the current. The net effect of the vortical structures on the concentration (density) field was seen in figure 4.

4 SUMMARY AND CONCLUSIONS

In this work we present highly resolved 3D simulations of cylindrical density currents performed at three different $Re = 895$, 3450, and 8950. The particular choice of $Re = 3450$ corresponds to a Grashof number $Gr = 1.5 \times 10^6$, the dimensionless parameter used by Härtel et al. (2000b) in their planar current simulations. The other two Re correspond to $Gr = 10^5$ and

$Gr = 10^7$. The simulations have been conducted with a de-aliased spectral code. This highly accurate numerical formulation allows the capture of all relevant length scales present in the flow.

The objective of the study is to examine the structure and dynamics of cylindrical density currents. As the front spreads, a shear layer forms between the heavy forward advancing and the light backward retreating fronts. As the interface develops between the two fronts, it rolls up forming Kelvin-Helmholtz vortices. The dynamic of the interface is highly dependent on the Reynolds number of the flow. For the lower Reynolds analyzed in this work, only one vortex is formed, which remains axisymmetric during all the duration of the simulation. The interface stays smooth and nearly horizontal behind the front. For the larger two Reynolds numbers considered, the interface evolves more dynamically. Firstly, more Kelvin-Helmholtz vortices are formed as the front advances: for $Re = 3450$ three vortices are formed while for $Re = 8950$ four are formed. In these cases, the vortices are destabilized in the azimuthal direction and eventually decay into smaller scale vortices. High turbulence in the flow is associated to regions where this process occurs, and as a consequence, the interface is very irregular with large undulations. For $Re = 8950$ the flow is strong enough to promote vortex pairing between the shed Kelvin-Helmholtz vortices.

The interface roll-up is not sustained during all the duration of the flow. Assuming a scaling law $\overline{u}_F \sim \tilde{t}^{\beta}$ for the front velocity of a cylindrical current, the net circulation across the interface can be estimated as $\Gamma(\tilde{t}) \sim \overline{u}_F(\tilde{t})\overline{l}_F \sim \tilde{t}^{2\beta+1}$. Thus, circulation is sustained over time only for $\beta > -1/2$, during the slumping phase of spreading in which $\beta \sim 0$. During the intermediate inertial phase $\beta = -1/2$ and circulation remains constant. During the final viscous phase $\beta = -3/4$ (Hoult, 1972) or $-7/8$ (Huppert, 1982) if the viscous effects are associated to interface shear or bottom friction, respectively. Then, circulation decreases with time and no new vortex are formed.

Along with the formation of Kelvin-Helmholtz vortices at the interface, a series of counter-rotating vortices forms at the bottom boundary. Each counter-rotating vortex is associated with a Kelvin-Helmholtz vortex, and their eventual interaction results on the dissipation of the counter-rating vortex, and the lift up and retardation of the original Kelvin-Helmholtz vortex. The retardation of the first Kelvin-Helmholtz vortex formed at the leading front results in the formation of another vortex, marked A5 in the figures. As the flow evolves, these two vortices may or may not pair, but nevertheless, they both form the head of the current.

For the larger two Reynolds number flows, a clear pattern of lobes and clefts develops. The minute perturbations in the initial condition grow very fast, originally at the lower part of the leading front, but very rapidly extend to the upper and rear part of the front. In the case of the lower Reynolds flow, the perturbations are not amplified and the flow progresses axisymmetrically. After lobes and clefts are formed, they evolve very dynamically presenting merging of clefts and splitting of lobes into new ones. The process is similar for both larger Reynolds numbers, however, the larger Reynolds flow is characterized by smaller scales. The wavelength of the lobes grows with time as the front spreads and the local Reynolds number of the flow decreases. This is consistent with previous studies on planar currents that show that the most unstable wavelength decreases with the Reynolds of the flow (Härtel et al., 2000a).

Laboratory experiments for the larger Reynolds were performed in order to compare with the numerical simulations. Although the setting of the experiments is not exactly as the simulations, front velocity and lobes wavelength from numerical results and experimental observations agree very well. The experiments were performed with salt water spreading in quiescent fresh water. The Schmidt number for this experiment is 700, while for the numerical simulations is 1. This

offers some justification to findings that as long as $Sc > \mathrm{O}(1)$ the flow and the lobe and cleft pattern are not very sensitive to the precise value of Sc (Härtel et al., 2000b; Cantero et al., 2006a).

As mentioned above, regions of high turbulence in the flow are associated to Kelvin-Helmholtz vortices. These regions are populated with trains of hairpin vortices tilted toward the axis. Similar findings have been reported by Cantero et al. (2006b) for planar currents, however, in that case the hairpin vortices are distributed evenly all over the head and body of the current.

5 ACKNOWLEDGEMENTS

We gratefully acknowledge the support of the Marine Geophysics Program of the Office of Naval Research, the Chicago District of the US Army Corps of Engineers, and the Metropolitan Water Reclamation District of Greater Chicago. Support from the National Center for Supercomputer Applications (NCSA) at the University of Illinois at Urbana-Champaign (UIUC) is also acknowledged. Mariano Cantero was supported by a Graduate Student Fellowship from the Computational Science and Engineering Program at UIUC. Dr. James Ferry collaborated in the early stages of the computations. Computer time was partially provided by Dr. Nahil Sobh and Dr. Fady Najjar. Dr. Gregory Bower from NCSA helped to solve memory issues to run the larger simulation. Dr. David Bock from NCSA produced visualization of the larger simulation.

REFERENCES

A. Alahyari and E. Longmire. Development and structure of a gravity current head. *Experiments in Fluids*, 20:410–416, 1996.

J. Allen. Mixing at turbidity current heads, and its geological implications. *Journal of Sedimentary Petrology*, 41(1):97–113, 1971.

J. Allen. *Principles of Physical Sedimentology*. George Allen and Unwin Ltd, 1985.

R. Bonnecaze, M. Hallworth, H. Huppert, and J. Lister. Axisymmetric particle-driven gravity currents. *Journal of Fluid Mechanics*, 294:93–121, 1995.

M. Cantero, S. Balachandar, M. García, and J. Ferry. Direct numerical simulations of planar and cyindrical density currents. *Journal of Applied Mechanics*, page in press, 2006a.

M. Cantero, J. R. Lee, S. Balachandar, M. García, and M. Y. Ha. On the front velocity of gravity currents. *Journal of Fluid Mechanics*, page under review, 2006b.

P. Chakraborty, S. Balachandar, and R. Adrian. On the relationships between local vortex identification schemes. *Journal of Fluid Mechanics*, 535:189–214, 2005.

T. Fannelop and G. Waldman. The dynamics of oil slicks – or 'creeping crude. *A.I.A.A. J.*, 41: 1–10, 1971.

J. Fay. The spreads of oil slicks on a calm sea. In David P. Hoult, editor, *Oils in the sea*, pages 53–63, 1969.

M. García and J. Parsons. Mixing at the front of gravity currents. *Dynamics of Atmospheres and Oceans*, 24:197–205, 1996.

M. Hallworth, H. Huppert, J. Phillips, and R. Sparks. Entrainment into two-dimensional and axisymmetric turbulent gravity currents. *Journal of Fluid Mechanics*, 308:289–311, 1996.

M. Hallworth, H. Huppert, and M. Ungarish. Axisymmetric gravity currents in a rotating system: experimental and numerical investigations. *Journal of Fluid Mechanics*, 447:1–29, 2001.

C. Härtel, F. Carlsson, and M. Thunblom. Analysis and direct numerical simulation of the flow at a gravity-current head. Part 2. The lobe-and-cleft instability. *Journal of Fluid Mechanics*,

418:213–229, 2000a.

C. Härtel, E. Meiburg, and F. Necker. Analysis and direct numerical simulation of the flow at a gravity-current head. Part 1. Flow topology and front speed for slip and no-slip boundaries. *Journal of Fluid Mechanics*, 418:189–212, 2000b.

D. Hoult. Oil spreading in the sea. *Ann. Rev. Fluid Mechanics*, 4:341–368, 1972.

H. Huppert. The propagation of two-dimensional and axisymmetric viscous gravity currents over a rigid horizontal surface. *Journal of Fliud Mechanics*, 121:43–58, 1982.

H. Huppert and J. Simpson. The slumping of gravity currents. *Journal of Fluid Mechanics*, 99: 785–799, 1980.

B. Lee and R. Wilhelmson. The numerical simulation of non-supercell tornadogenesis. Part I: Initiation and evolution of pretornadic misocyclone circulation along a dry outflow boundary. *Journal of the Atmospheric Sciences*, pages 32–60, 1997a.

B. Lee and R. Wilhelmson. The numerical simulation of non-supercell tornadogenesis. Part II: Evolution of a family of tornadoes along a weak outflow boundary. *Journal of the Atmospheric Sciences*, pages 2387–2415, 1997b.

B. Marino, L. Thomas, and P. Linden. The front condition for gravity currents. *Journal of Fluid Mechanics*, 536:49–78, 2005.

F. Necker, C. Härtel, L. Kleiser, and E. Meiburg. High-resolution simulations of particle-driven gravity currents. *International Journal of Multiphase Flow*, 28:279–300, 2002.

T. Özgökmen, P. Fischer, J. Duan, and T. Iliescu. Three-dimensional turbulent bottom density currents from a high-order nonhydrostatic spectral element model. *Journal of Physical Oceanography*, 34:2006–2026, 2004.

J. Parsons and M. García. Similarity of gravity current fronts. *Physics of Fluids*, 10(12):3209–3213, 1998.

M. Patterson, J. Simpson, S. Dalziel, and G. van Heijst. Vortical motion in the head of an axisymmetric gravity current. *Physics of Fluids*, 18(4), 2006.

J. Rottman and J. Simpson. Gravity currents produced by instantaneous releases of a heavy fluid in a rectangular channel. *Journal of Fluid Mechanics*, 135:95–110, 1983.

J. Simpson. Effects of the lower boundary on the head of a gravity current. *Journal of Fluid Mechanics*, 53(4):759–768, 1972.

J. Simpson. *Gravity Currents*. Cambridge University Press, second edition, 1997.

J. Simpson and R. Britter. The dynamics of the head of a gravity current advancing over a horizontal surface. *Journal of Fliud Mechanics*, 94:477–495, 1979.

J. Zhou, R. Adrian, S. Balachandar, and T. Kendall. Mechanics for generating coherent packets of hairpin vortices. *Journal of Fluid Mechanics*, 387:353–396, 1999.

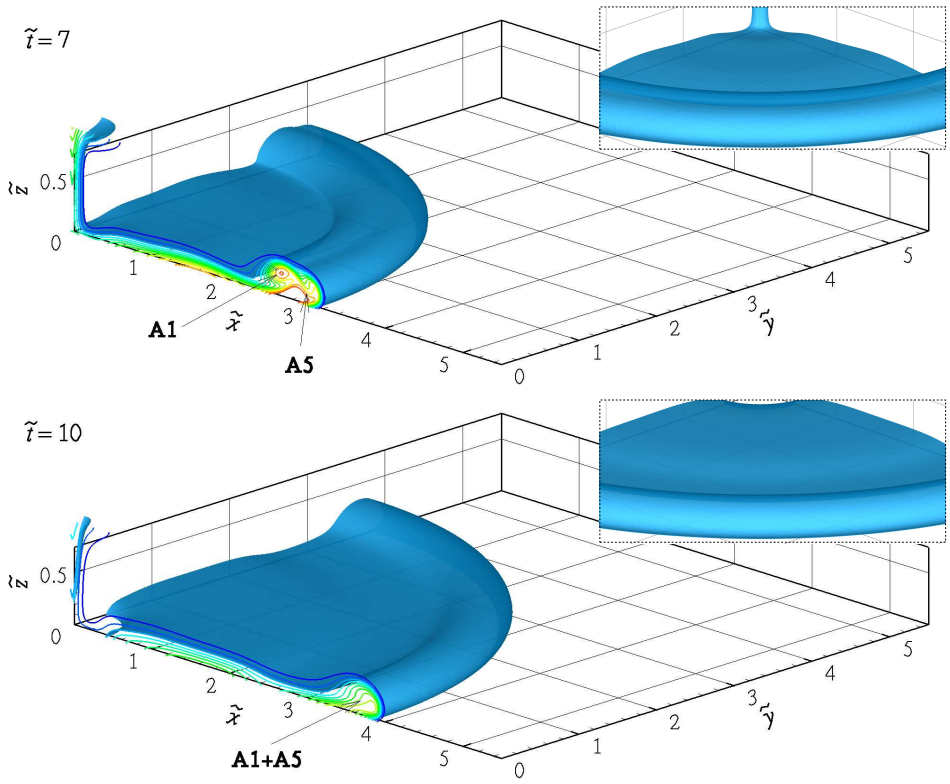

Figure 2: Flow visualized by isosurface of $\tilde{\rho} = 0.15$ for $Re = 895$. The figure shows only one quadrant of the computational domain. The head consists of two coherent anti-clockwise rotating vortex rings marked A1 and A5 on the $\tilde{x} - \tilde{z}$ plane. For this Re the flow progresses axisymmetrically. The insets show a front view of the flow.

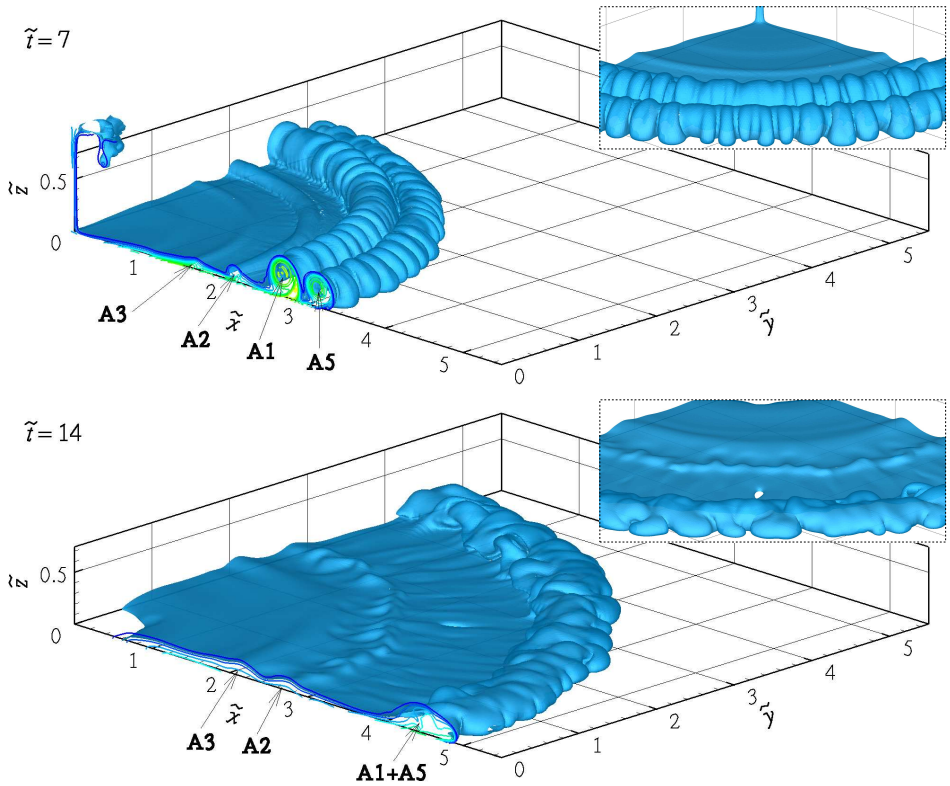

Figure 3: Flow visualized by isosurface of $\tilde{\rho} = 0.15$ for $Re = 3450$. The figure shows only one quadrant of the computational domain. The interface rolls up and forms three vortex rings marked A1, A2 and A3 on the $\tilde{x} - \tilde{z}$ plane. Then A5 is formed, which eventually merges with A1 to form the head of the current at later times. For this Re, the front instabilities of the initial condition grow with time and form a pattern of lobes and clefts. The insets show a front view of the flow.

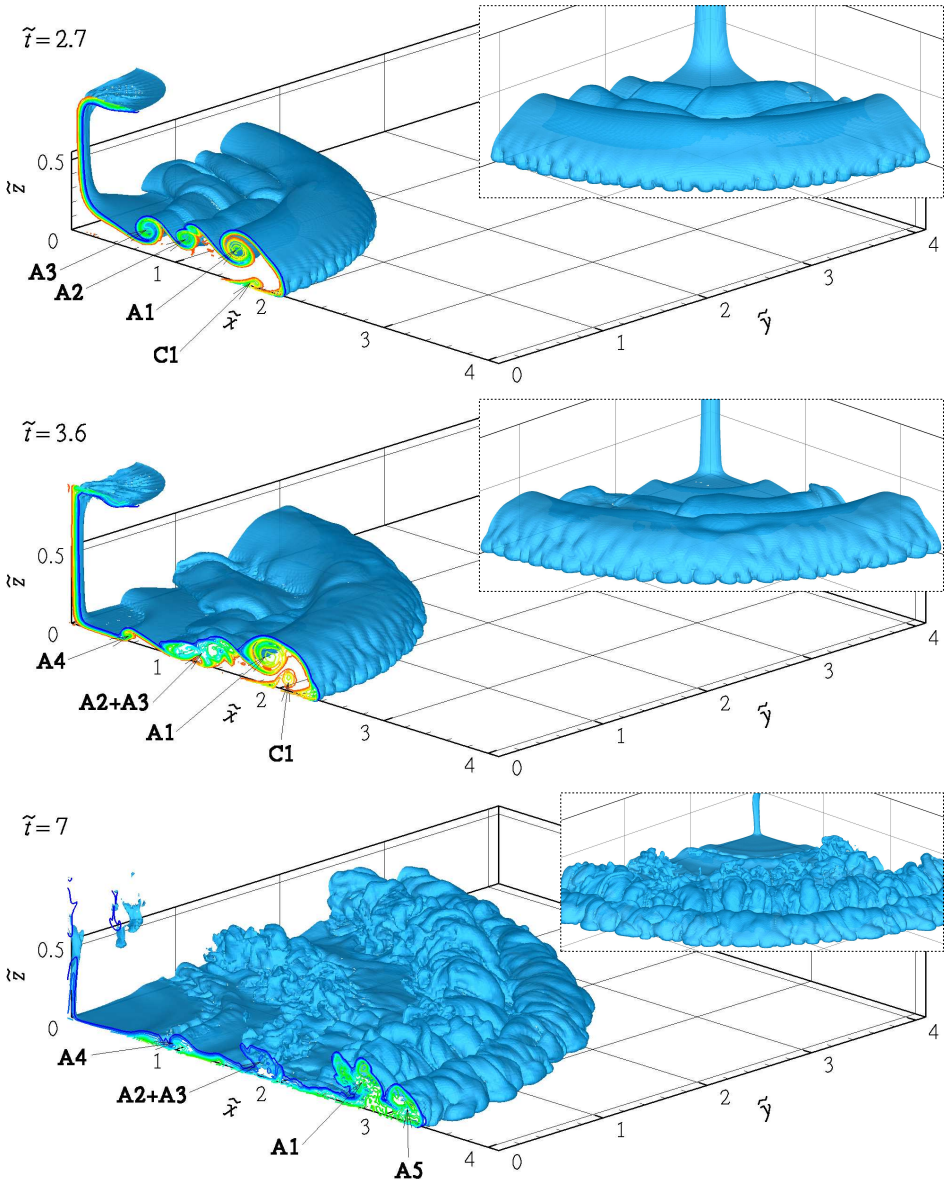

Figure 4: See caption in figure 4, frames for $\tilde{t} = 14$ and 21.

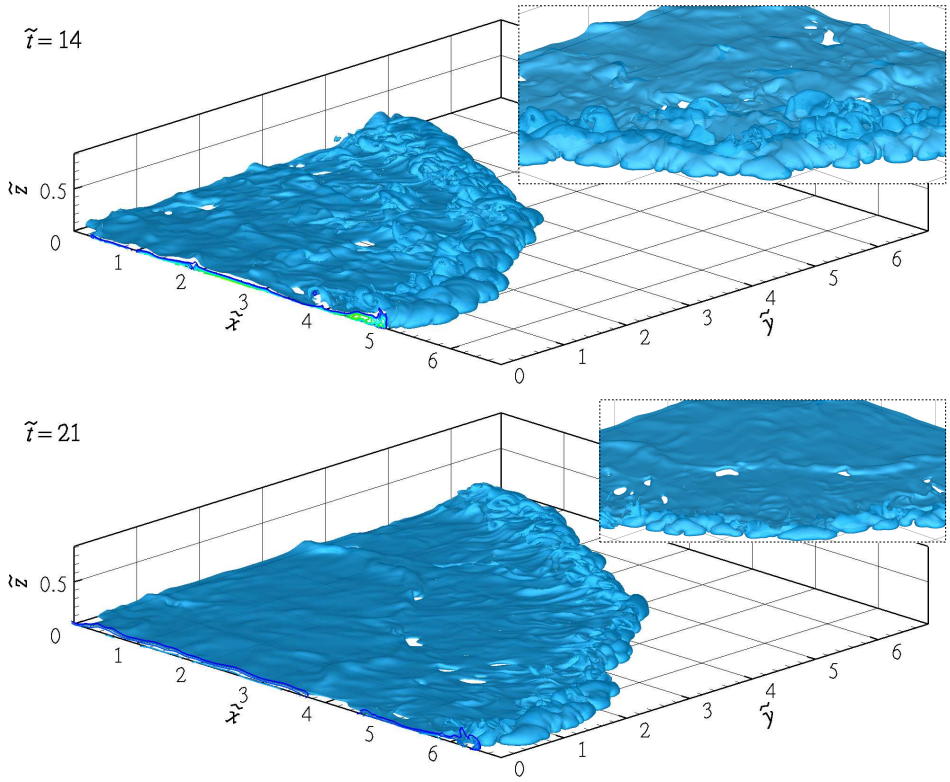

Figure 4: Flow visualized by isosurface of $\tilde{\rho} = 0.15$ for $Re = 8950$. The figure shows only one quadrant of the computational domain. Initially, the flow evolves axisymmetrically. Kelvin-Helmholtz vortex rings develop forming the front and body of the current marked A1, A2, A3 and A4 on the $\tilde{x}-\tilde{z}$ plane. Then A5 is formed, which eventually merges with A1 to form the head of the current at later times. Later, three-dimensionality develops and destabilize the vortex rings in the azimuthal direction which decay to smaller scale turbulence. Eventually, the Kelvin-Helmholtz vortex decay and the body of the current becomes a calm region where most of the flow manifest as interfacial waves. For this Re, the front instabilities of the initial condition grow very rapidly with time and form a pattern of lobes and clefts. The insets show a front view of the flow.

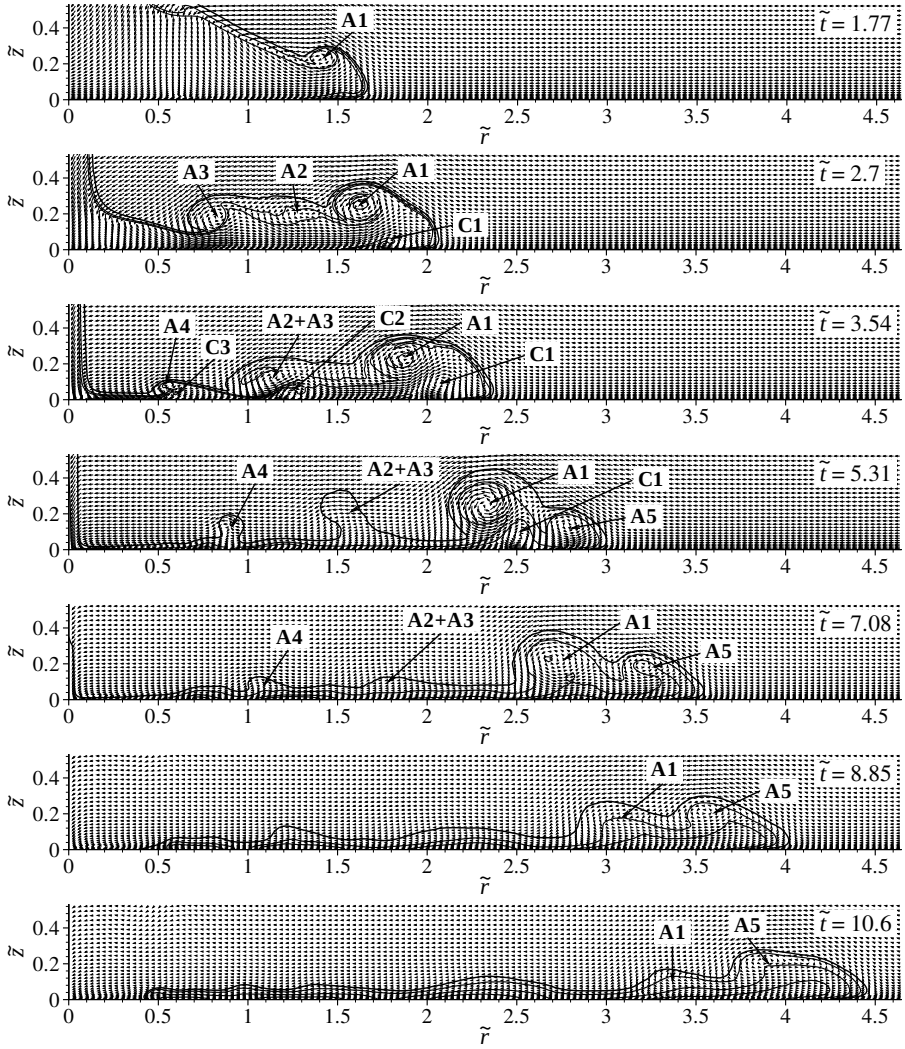

Figure 5: Flow field visualized by circumferentially-averaged velocity vectors. To allow for better vortex visualization, the nose velocity has been subtracted in each frame. The current interface is visualized by the contour of $\tilde{\rho} = 0.15$. Density contours are also shown to help visualize the current structure.

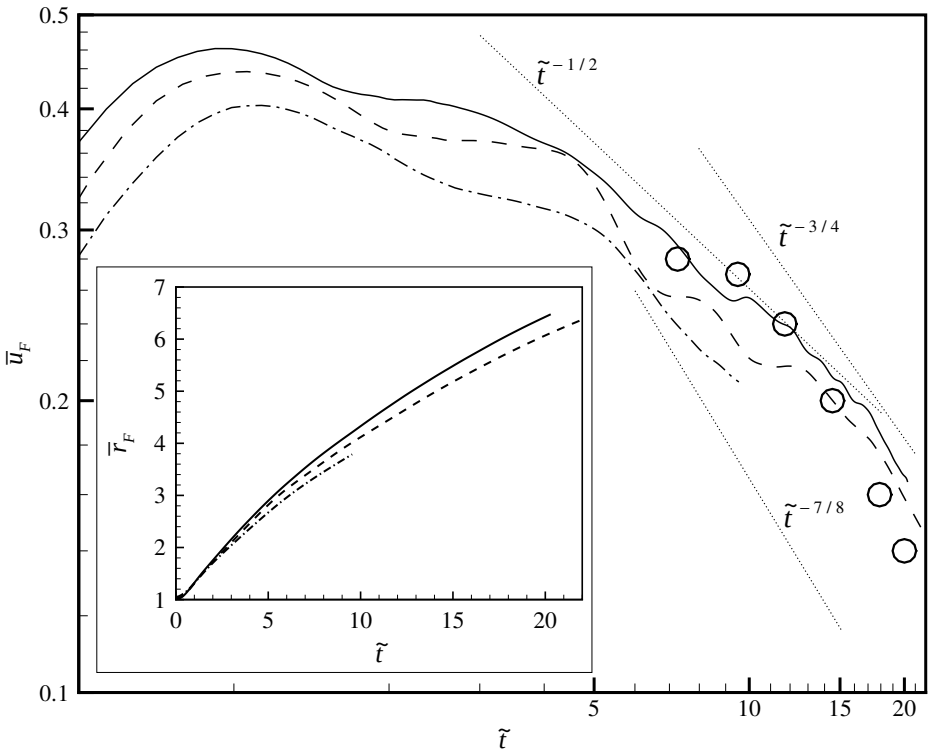

Figure 6: Front velocity as function of time. The plot is in log-log scale. Inset shows front location as a function of time. Solid line: $Re = 8950$, dashed line: $Re = 3450$ and dashed-dot line: $Re = 895$. Circle: data from experiment for $Re = 8950$.

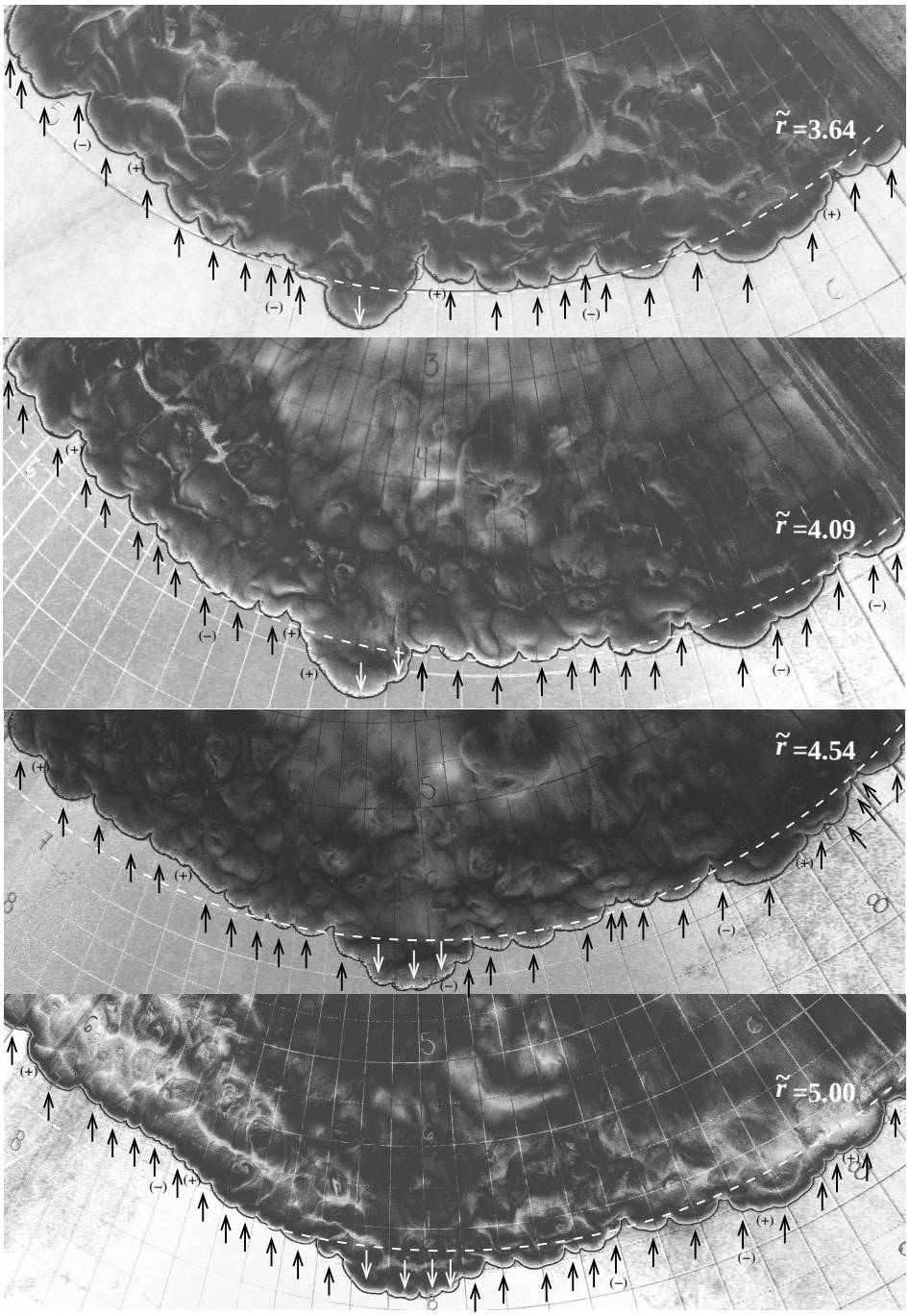

Figure 7: Lobes and cleft from an experiment for $Re = 8950$ and $Sc = 700$. Each frame shows the entire front in the experiment which extend a circular section of $\pi/2$. From top to bottom, the frames correspond to time instances when the front is locate at $\tilde{r} = 3.6$, 4.1, 4.5 and 5.0, respectively. Through postprocessing the lobe-and-cleft pattern has been demarcated in the pictures. Each lobe is indicated with an arrow. Locations where a lobe is not clearly seen and it was not counted (but could still have been counted) are demarcated with an (+) sign. On the other hand, locations where a lobe has been counted but was not clearly seen are demarcated with a (-) sign. In this way, an error can be estimated in the number of lobes counted.

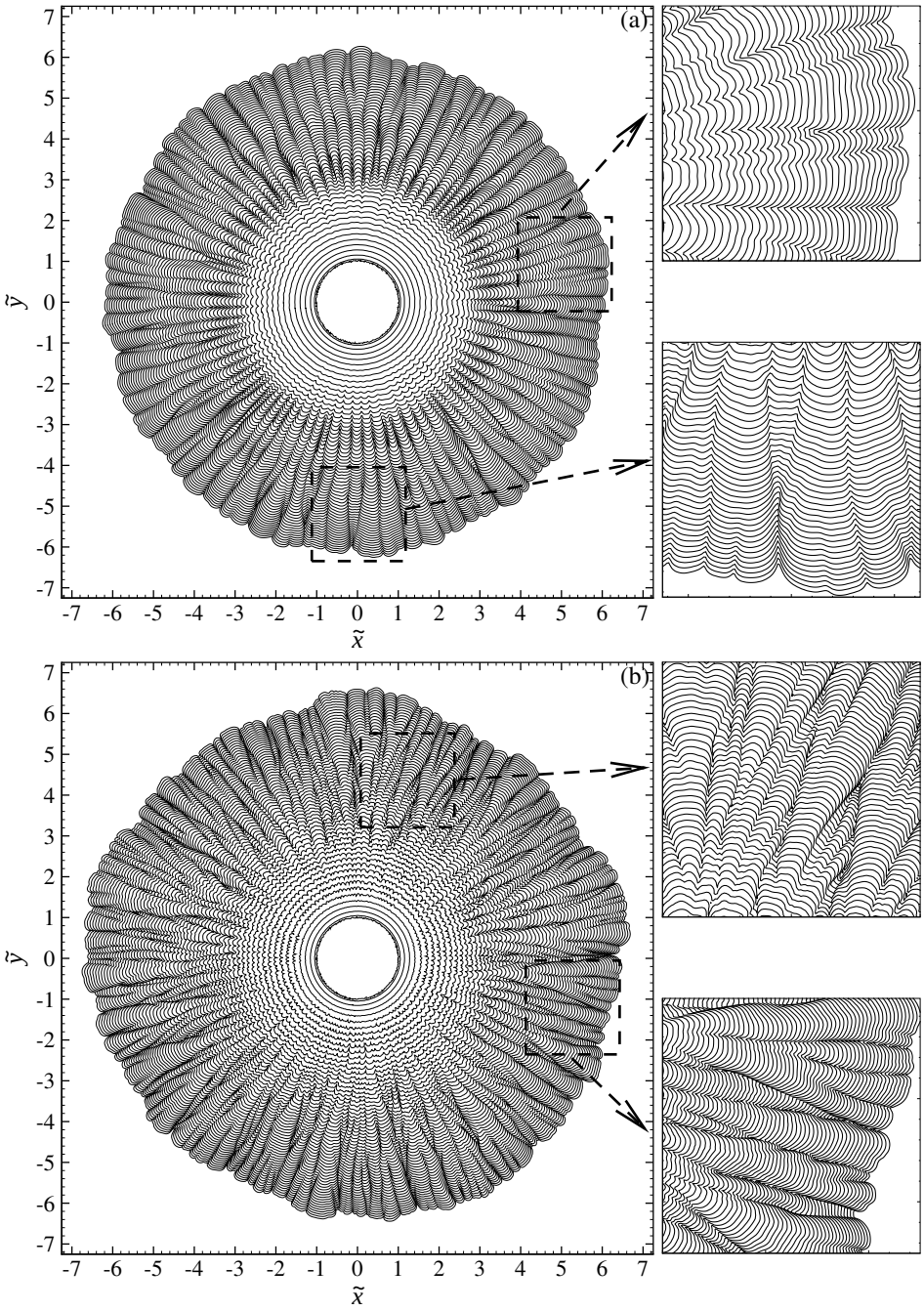

Figure 8: Composite picture of the front location over time. Front visualized by bottom contour of $\tilde{\rho} = 0.015$. The time separation between contour is $\Delta\tilde{t} = 0.354$. The details show several lobe splitting and merger. Frame (a): $Re = 3450$, and frame (b): $Re = 8950$.

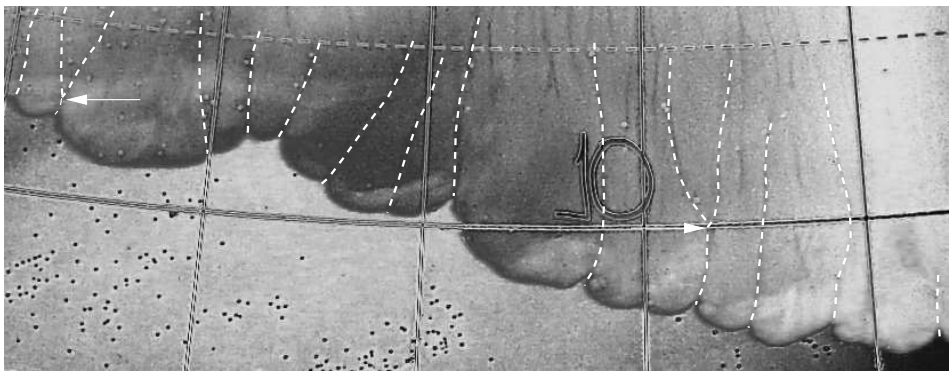

Figure 9: Detail of lobes and cleft from an experiment for $Re = 8950$ with $Sc = 700$. The front is located at $\tilde{r} \simeq 6.5$. At this time the concentration of potassium permanganate at the front has decreased enough to allow the visualization of cleft by streaks of fresh clear water trapped between the bottom boundary and the current in the near-front region. These streaks has been demarcated in the figure with dashed lines to help their visualization. Two merger of clefts (marked with arrows) can be observed in the figure. Compare to figure 8.

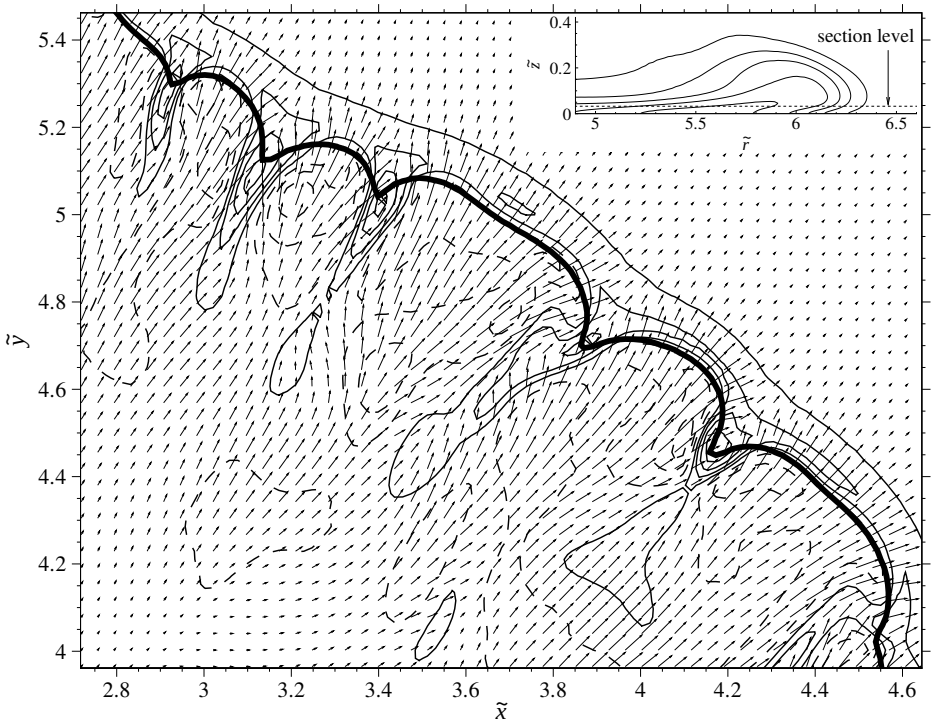

Figure 10: Near-bed flow at the front of the current for $Re = 3450$ at $\tilde{t} = 21$. The inset indicates the location of the section at $\tilde{z} = 0.04$ relative to the front. The front is visualized by the corresponding bottom density contour of $\tilde{\rho} = 0.015$ (thick solid line). The vector field shows the horizontal flow (velocity components $\tilde{u}_x$ and $\tilde{u}_y$) and the contour lines show the vertical flow (solid line: positive $\tilde{u}_z$, and dashed line: negative $\tilde{u}_z$). By the vector field it can seen that the horizontal flow in the clefts is slower that in the lobes. It is clear also, that there is a circumferential horizontal flow from the center of the lobes into the clefts. The vertical flow is upwards (solid line contours) at the cleft locations and downwards at the lobes location (dashed line contours).

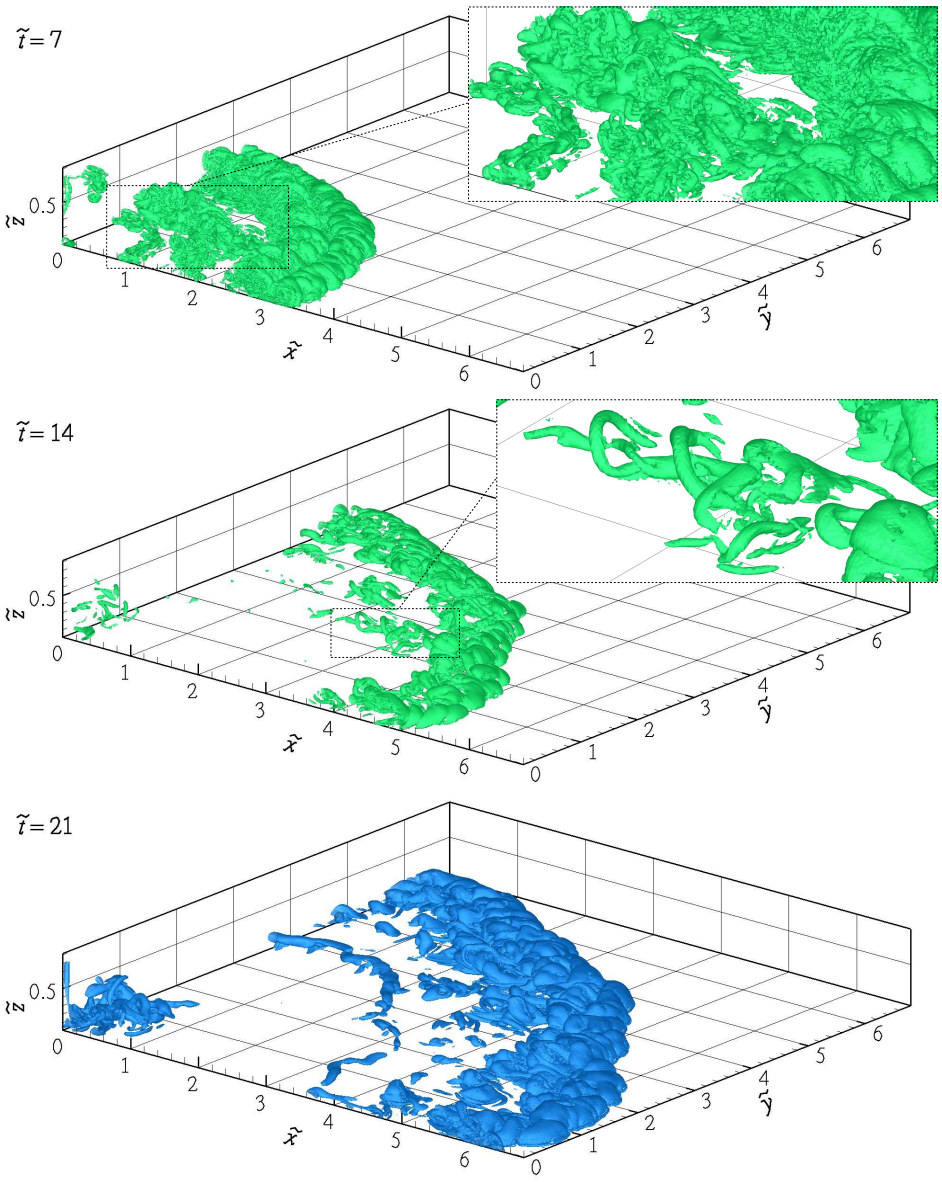

Figure 11: Flow structures visualized by an isosurface of $\tilde{\lambda}_{ci}$. For $\tilde{t} = 7$ and 14 the isosurface of $\tilde{\lambda}_{ci} = 2.12$ is shown, while for $\tilde{t} = 21$ the isosurface of $\tilde{\lambda}_{ci} = 0.35$ is shown The insets show detailed view. The inset in frame for $\tilde{t} = 14$ shows in detail a train of asymmetric hairpin vortices that have formed behind the front.